Time-Resolved, Multi-frame X-Ray Imaging
of Laser-Produced Plasmas

L. A. Gizzi, A. Giulietti, and O. Willi*

*Istituto di Fisica Atomica e Molecolare del CNR, Pisa, Italy; and *Imperial College of Science,
Technology and Medicine, London, England*

A novel x-ray imaging system based on a microchannel-plate combined with a multi-pinhole camera has been employed to study x-ray emission from laser-produced plasmas in the 0.5–3 keV photon energy range. In particular, the interaction of intense laser radiation with such plasmas, under conditions relevant to inertial confinement fusion, was monitored by recording a sequence of consecutive x-ray images with a temporal resolution of 140 ps and a spatial resolution of 10 μm. These images provide valuable information on the main physical mechanisms involved in the interaction process, including collisional absorption of the incident laser energy and electron thermal conduction. © 1997 Academic Press

1. INTRODUCTION

The study of plasma self-emission in the x-ray region is widely regarded as a primary tool for the characterisation of hot, dense plasmas generated in laser–matter interaction processes. Indeed, in the case of experiments designed to investigate laser–plasma coupling processes or hydrodynamic laser induced instabilities in the interaction with performed plasmas, a detailed analysis of the spectral and spatial features of the x-ray emission allows a direct monitoring of the modifications induced by the interaction processes on plasma conditions (1). On the other hand, x-ray imaging with high temporal resolution is also considered the key diagnostic technique to study the overall dynamics and the evolution of distortions in the implosion of inertial confinement fusion capsules (2).

Due to the strong x-ray emissivity of laser produced plasmas, a simple imaging device consisting of a pinhole camera (PHC) can be employed to obtain x-ray images of the plasma. Both magnification and resolution of such a device can be easily calculated from simple geometrical consideration. The image thus obtained can be recorded directly by using x-ray sensitive detectors (windowless CCD cameras, x-ray films) or by employing phosphor screens coupled to optical image intensifiers. Presently available intensifiers based on the microchannel-plate (3) (MCP) technology can easily provide a thousandfold overall gain in intensity. Ordinary CCD cameras or commercial photographic black-and-white film can then be used to record the intensified image.

Temporal resolution can be achieved by forming the x-ray image generated by the PHC on a position sensitive time resolving device. By using an x-ray streak camera, temporal resolution up to the picosecond range can be obtained. However the spatial

information is restricted to the direction perpendicular to the streak direction (1-D time-resolved imaging). This technique has been successfully employed for several years (4) and is very useful when a continuous mapping of the temporal evolution is required. However, two-dimensional position sensitive devices with a temporal resolution as high as a few tens of picosecond based on *microchannel-plates* (MCP) (5) can now be employed. MCPs are characterised by a very low capacitance that enables fast switching of the externally applied electric fields. These devices can therefore be used as *gated intensifiers* as well as DC intensifiers and usually do not require additional intensifiers due to their intrinsic high gain.

In all the applications considered above, in order to avoid motional blurring of the images, framing times as short as few tens of picoseconds (6) are often necessary. On the other hand, the scalelength of the features of interest can be as small as few micrometers, thus accounting for the need of high spatial resolutions. Furthermore, another important feature of such imaging systems is the number of frames that can be recorded on a single interaction event, so that the temporal evolution can be mapped with sufficient accuracy. The final configuration is therefore a trade-off between scientific requirements, spatial, temporal and spectral accuracy on one side, and flexibility, reliability, and ease of use on the other side.

In this paper we describe the implementation of multi-frame x-ray imaging with high temporal resolution for the study of laser interaction with preformed plasmas. A detailed description of the technique will be given here with emphasis on its application to the investigation of laser–plasma coupling processes. The interaction of a high intensity laser pulse with preformed plasmas, generated by laser heating of thin Al foils, was investigated by means of this diagnostic, in conditions of temperature, density and laser intensity typical of inertial confinement fusion experiments.

2. IMAGING TECHNIQUE

An x-ray detection unit based on MCP, in the following referred to as SLIX (strip line imager for x rays), was designed (7) to enable four-frame x-ray imaging with 140 ps gate-time and inter-frame time adjustable from zero to a few nanoseconds. A diagram of the SLIX sensitive unit is shown in Fig. 1. The input surface of the microchannel-plate detector was coated with a 500-nm copper layer in four separated rectangular regions (strip lines) acting as photocathodes while the output surface was uniformly coated with a thin copper layer. Each strip line could be activated independently by a high voltage pulse. Photons incident on one of the activated strip lines generates photoelectrons that, accelerated by the external electric field, hit the walls of the microchannel producing secondary electron emission. This process takes place several times during the flight of the electrons in the microchannel resulting in a photomultiplier-like gain. The electrons produced are finally driven onto a phosphor screen by a second electric field. Due to the small electron path lengths (see Fig. 1), a relatively large electric field is capable of preserving the spatial distribution of the outcoming electrons. A standard black-and-white film records the light produced by the phosphor screen and collected by a fibre optic bundle plate.

A specifically designed PHC equipped with a 4-pinhole array capable of producing four identical images of the object plasma onto the four sensitive strip lines of the
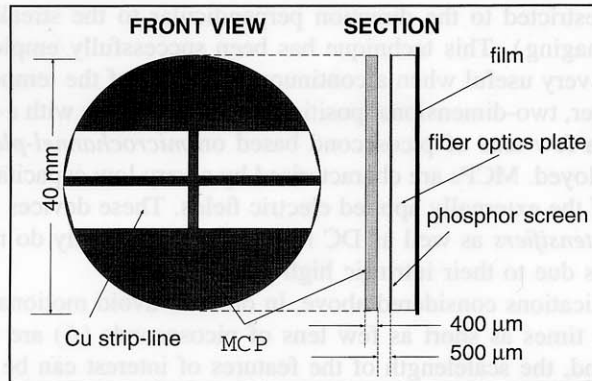
FIG. 1. Schematic arrangement of the strip-line x-ray imager detection system with the MCP input surface showing the four 500-nm-thick Cu coated regions. (Kentech Instr. Ltd., UK.)

MCP was employed as schematically shown in Fig. 2. The 4-pinhole array was made by piercing the four pinholes on a 30-μm-thick platinum foil using a Q-switched 40 ns Nd laser beam focused onto the foil by a microscope objective. The PHC magnification in the final setup used for the experiment described below was 13$\times$ with a pinhole size of 10 μm. Both magnification and pinhole size were chosen in order to resolve details of about 10 μm in the plasma. Since the intrinsic SLIX spatial resolution, determined by the MCP structure, is about 100 μm, the 13$\times$ image magnification allows the limit resolution (10 μm) of the PHC imaging system, set by the pinhole diameter, to be attained.

3. SPECTRAL X-RAY SELECTION

In our experiment the time-resolved imaging was mainly devoted to investigate modifications of plasma condition induced by local energy deposition. Such modifications occur on a time scale which is short compared to the typical time scale of relaxation of atomic physics processes. To this purpose continuum emission is a more
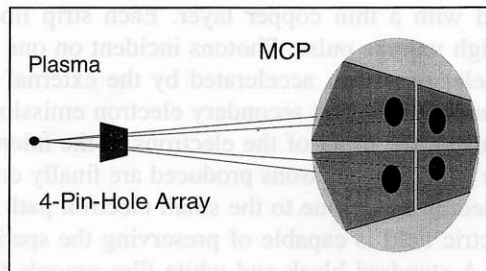

FIG. 2. Schematic set-up of the imaging system showing the pin-hole set arrangement and the input window of the four-frame gated x-ray imager SLIX. The geometry of the pin-hole array was defined by the image magnification in order to produce four images centered on the four sensitive areas of the detector.
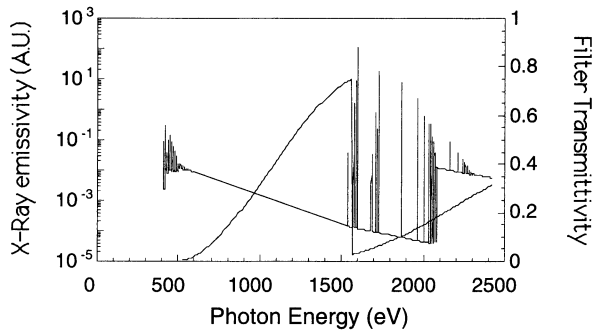
FIG. 3. X-ray transmittivity of the 3 μm Al filter used in the SLIX imaging system. The x-ray emissivity of a 450 eV, 1.5×10^{20} cm^{-3} Al plasma in collisional-radiative equilibrium is also plotted for comparison.

sensitive parameter compared to line emission. In fact, continuum radiation and, in particular, radiation originating from free–free processes, is closely related to the conditions of the electron population and is only coupled to the ions via their charge number and the electron–ion collision frequency. In contrast, the properties of line radiation are strongly related to the particular equilibrium holding in the plasma, as well as to ion relaxation processes.

For this reason a 3-μm-thick Al foil filter was used to block visible radiation as well as to select the transmitted x-ray spectrum. Figure 3 shows the transmittivity of the 3-μm Al filter in the spectral range of interest in this study. Also plotted on the same graph is the expected x-ray spectral emissivity of the plasma calculated by using the atomic physics code RATION (8), assuming a collisional–radiative equilibrium, for an Al plasma at an electron density of 1.5×10^{20} cm^{-3} and an electron temperature of 450 eV. These values were chosen according to experimental measurements performed in similar experimental conditions and described in detail elsewhere (9). Due to the Al K-shell absorption edge at 1560 eV, most of the line emission from He-like and H-like Al ions is strongly absorbed by the Al filter. Therefore the dominant component of the transmitted x rays will be continuum radiation originating from free–bound and free–free transitions in He-like and H-like Al ions, as discussed above.

4. EXPERIMENTAL RESULTS

Plasmas were produced by irradiating targets consisting of a 800-nm-thick Al stripe (300 μm wide, 500 μm long) coated onto a 0.1-μm-thick plastic substrate as shown schematically in Fig. 4. Four frequency doubled laser beams ($\lambda_0 = 0.532$ μm, FWHM = 600 ps) of the Vulcan laser at the Central Laser Facility (Rutherford Appleton Laboratory, Chilton, Didcot, UK) were superimposed on target, two on each side, in order to generate and heat the plasma. The dashed ellipse around the Al coating shows schematically the size of the focal spot of the four heating beams. A fifth infrared laser beam ($\lambda_0 = 1.064$ μm, FWHM = 600 ps) was then focused on the target along its longitudinal axis using an f/10 optics as shown in Fig. 4 and was timed to reach the target typically between 2 and 3 ns after the peak of the plasma forming beams.

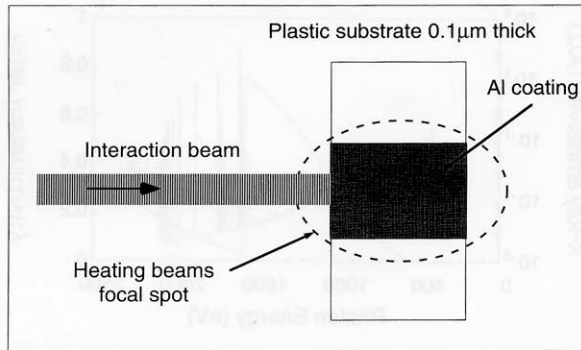Figure 5 shows a time integrated pinhole x-ray image of the target heated with 600

FIG. 4. Target configuration and laser beams arrangement for the production of laser plasmas. The Al coating was either 500 or 700 nm thick. The Al target was 300 μm wide and 500 μm long (along the interaction beam axis). The preformed plasma is created from the laser-heated exploding foil and expands perpendicularly to the foil plane.

ps, 0.53 μm laser pulses at an intensity of $\approx 2 \times 10^{13}$ W/cm^2 on each side, obtained with the SLIX working as a DC x-ray intensifier. The 600-ps interaction pulse was delayed by 2.2 ns with respect to the heating pulses and was focused on the (left) edge of the foil target at an intensity approximately 10^{13} W/cm^2, in a 140 μm (FWHM) focal spot using an f/10 optics. The shape of the bright x-ray emitting region, even though integrated in time, clearly matches the shape of the Al heated target as shown in Fig. 4. This observation suggests that most of the x-ray emission occurs during the plasma startup phase, before hydrodynamic expansion takes place.
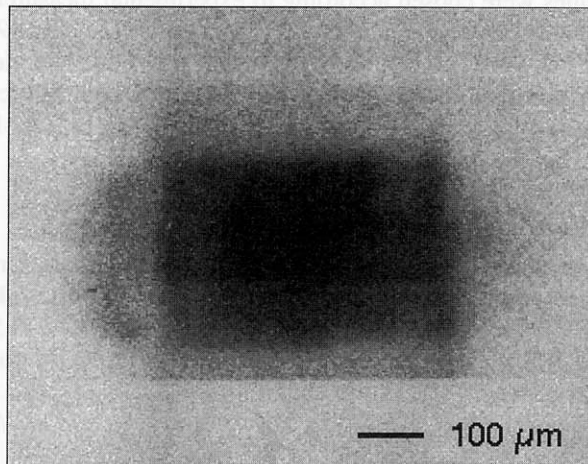

FIG. 5. Time integrated X-ray image of a 700 nm thick, 500 μm long, 300 μm wide Al target heated on each side by a 600 ps, 0.53 μm laser pulses at an intensity of $\approx 2 \times 10^{13}$ W/cm^2. The 600 ps interaction pulse was delayed by 2.2 ns and was focused on target at an intensity of approximately 10^{13} W/cm^2. The image was obtained with the SLIX working as a DC X-ray intensifier.
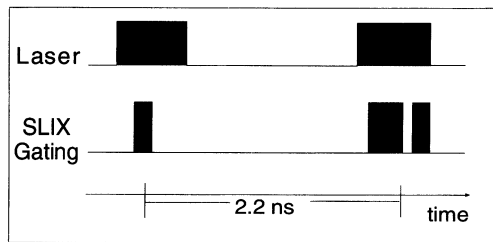
FIG. 6. Timing of the SLIX frames (1 to 4) relative to the timing of the laser pulses. The frame #1 was synchronized with the heating (H) pulse to monitor plasma formation. All the remaining three frames were synchronized with the interaction (I) pulse.

As a consequence, in time integrated images, the effects of the interaction occurring in the field of view of the Al stripe are masked by the intense x-ray emission occurring in the early stage of plasma formation. Therefore temporal resolution is needed when studying interaction effects.

Temporal resolution can be achieved by the SLIX device when a gate voltage is applied to each strip line. A 650 V, 200 ps FWHM pulse was used to generate an electric field of approximately 15 KV/cm in the MCP, which was added to a low DC bias voltage ($\leqslant$300 V). Due to the extremely nonlinear behaviour of the MCP output current with the applied electric field, the gain produced by the low DC electric field, by itself, is negligible. Nevertheless, once added to the 200-ps gating pulse, this DC field activates the gain of the MCP. On the other hand, by varying the DC voltage it is possible to adjust the overall MCP gain. The gate pulse generated by a single pulse generator was split into four identical pulses which were applied to the four strip lines by using high frequency cables. The length of each cable was varied in order to synchronise the four frames according to the timing of the laser pulses.

Images like the one shown in Fig. 5 were produced on each of the four frames of the SLIX and then, by driving the frames at different times, a temporal sequence of four x-ray images of the laser–plasma interaction region was recorded. The timing of each frame was set according to the particular configuration of the interaction experiment as shown schematically in Fig. 6. Typically the first frame was synchronised with the heating laser pulse while remaining three frames were usually synchronised at different times during the interaction laser pulse.

A sequence of time resolved x-ray images of the laser–plasma interaction region is shown in Fig. 7. The target was heated at an incident laser intensity of $\approx$4 $\times$ 10^{13} W/cm^2 on each side, while the intensity of the 600-ps interaction pulse was 5.8 $\times$ 10^{13} W/cm^2. As indicated in Fig. 6, frame #1 was synchronised with the peak of the 600-ps heating pulse while the remaining three frames (#2, 3, and 4) were timed consecutively to record the evolution of the interaction process with the preformed plasma. X-ray emission relative to the heating phase involves the whole Al target foil and, though very intense in the first frame, drops below the detection level of the x-ray imaging system in the following frames, that is, after $\approx$2 ns. This is consistent with the x-ray time resolved spectra taken under similar experimental conditions and presented in a previous work (10) in which a simple model of x-ray emissivity was
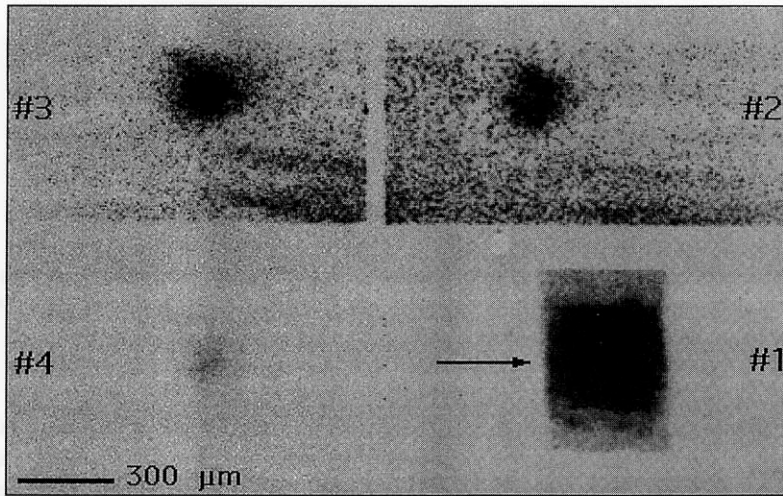
FIG. 7. Sequence of time-resolved x-ray images of laser interaction with a preformed plasma produced by irradiation of a 700-nm-thick, 300-μm-wide, 500-μm-long Al stripe at an intensity of $\approx 4 \times 10^{13}$ W/cm^2 on each side. The interaction beam was focused on the left edge of the plasma, as shown schematically by the arrow, in a 140 μm (FWHM) focal spot at an intensity of 5.8×10^{13} W/cm^2. The framing time was 120 ps, while the first interframe, that is the peak-to-peak delay between gate #1 and gate #2, was 2.2 ns, as shown in Fig. 6. The second and third interframes were zero and 100 ps respectively. The first frame, synchronized with the peak of the plasma heating pulse, shows x-ray emission from the plasma heating phase while the remaining three frames show the x-ray emission due to the interaction of the delayed laser pulse with the preformed plasma.

presented and discussed to explain the temporal behaviour of experimental x-ray emission.

X-ray emission takes place again when the interaction pulse strikes the preformed plasma. Such an emission is localised in a rather small region, close to the edge of the plasma, whose width (i.e., the size in the direction perpendicular to the direction of propagation of the laser beam and located in the plane of the target) is approximately 200 μm, that is, comparable with the focal spot size of the interaction beam (140 μm FWHM). On the other hand, the longitudinal size of the emission, once the effect of the angle of view (45°) between the imaging device and the target plane is taken into account, varies from 300 μm in the frame #2 to approximately 360 μm in the frame #3. The emissivity of this region rapidly decreases in time as shown by the weak image of frame #4 taken at the end of the laser interaction pulse. These circumstances, which make the interaction region ''visible'' in the x rays, indicate that a strong absorption of laser energy by the plasma takes place in this small region. According to detailed numerical simulations (7) the plasma electron density in this region is $n_e \cong 0.14 \ n_c$, where n_c is the critical density for the wavelength of the infrared interaction beam. In addition, the longitudinal density scalelength at the time of interaction is of the order of 100 μm; therefore, propagation of the interacting beam occurs without strong refraction and/or deflection effects. Under these conditions the main absorption process is the classical collisional absorp-

tion, i.e., inverse bremsstrahlung (IB), and electron heat transport accounts for propagation of the absorbed energy across the whole plasma. These physical mechanisms can be investigated by studying the features of x-ray emission for different plasma and laser conditions as discussed below.

5. PHYSICAL INSIGHTS

It is instructive to discuss briefly some aspects of the physics of laser–plasma interaction that should be taken into account in the analysis of the x-ray images presented above. In particular, absorption of laser energy by the plasma and electron heat transport will be considered as they play a very important role in determining the observed features of x-ray emission.

5.1. Inverse Bremsstrahlung Absorption

As already pointed out above, laser energy is transferred to the plasma mainly via IB absorption. Since most of the x-ray emission detected by our imaging system originates from electron–ion collision processes (bremsstrahlung and recombination), we expect strong x-ray emission from the region of plasma directly heated by the laser electric field, that is, from a region whose length is comparable with the IB absorption length. In other words, x-ray emission gives a good indication of the extent of plasma over which most of the laser energy is absorbed. Indeed, the longitudinal size of the x-ray emitting region measured from x-ray images was found to be in good agreement with the IB absorption length calculated for our plasma conditions assuming $T_e = 450$ eV and $n_e \cong 1.5 \times 10^{20}$ cm^{-3}.

We observe that, in the case of IB absorption, the absorption coefficient depends strongly ($\kappa_{ib} \propto n_e^2$) upon the electron density. Therefore, according to our model, the length of the x-ray emitting region is expected to increase strongly as the plasma electron density decreases. This effect was indeed observed experimentally performing interaction with a preformed plasmas characterised by a lower electron density. In fact, the preformed plasma was generated under the same experimental conditions of Fig. 7, but using a thinner Al target (500 nm thick instead of the 700 nm). In this case, the maximum electron density is expected (9) to be approximately 1.1×10^{20} cm^{-3} and the electron temperature is expected to be 400 eV, which is only slightly lower than in the previous case (450 eV). In this case, the absorption length is expected to be approximately 1 mm, that is, greater than the length of our preformed plasma. In fact, according to the frames #2 and #3 of Fig. 8, the longitudinal extent of the x-ray emitting region is indeed comparable to the length of the Al target. This result is in agreement with the conclusions of our simple model based on IB absorption and bremsstrahlung emission.

5.2. Heat Transport and X-Ray Emitting Region

Once the laser energy is absorbed as described above, it propagates over a volume determined by the characteristic thermal diffusion length. When the region of plasma directly heated by the laser is smaller than the diffusion length, thermal effects may play an important role in determining the size of the x-ray emitting region. Using a
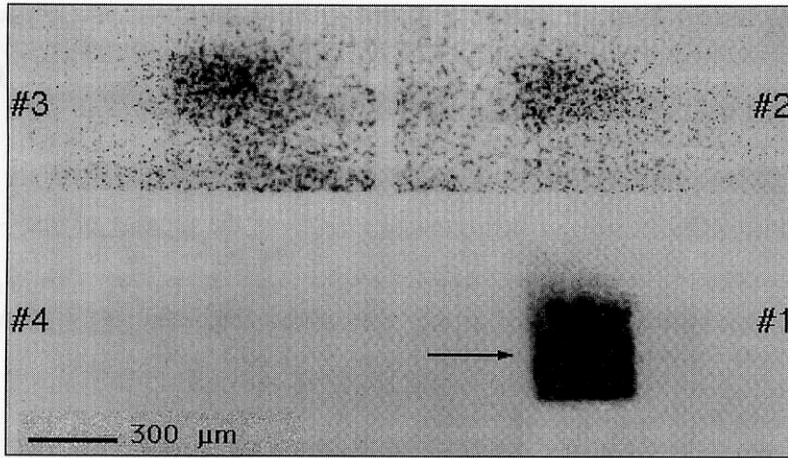
FIG. 8. Sequence of time resolved x-ray images of laser interaction with a preformed plasma. The interaction beam was focused on the left edge of the plasma, as shown schematically by the arrow, in a 140 μm (FWHM) focal spot at an intensity of 5.8×10^{13} W/cm². The framing time was 120 ps, while the first interframe, that is the peak-to-peak delay between gate #1 and gate #2, was 2.2 ns, as shown in Fig. 6. The second and third interframes were zero and 100 ps respectively. A lower density plasma at the time of interaction was obtained by using 500-nm-thick Al instead of the 700-nm-thick Al used in the case of Fig. 7. Due to the lower electron density of the preformed plasma, energy from the interaction pulse is absorbed over a much longer path than in the case of Fig. 7 (see text).

1-dimensional equation of classical thermal transport one can verify that the character-istic thermal diffusion length as a function of time t is given by $L_D \cong (\kappa_{SH} t / n_e)^{1/2}$, where $\kappa_{SH} \propto n_e \nu_t^2 \tau_e$ is the Spitzer–Härm conductivity (11) expressed in terms of the electron density, thermal velocity, and collision frequency. In the case of our experiment, assuming a fully ionised Al plasma at an electron temperature and density of 450 eV and 1.5×10^{20} cm^{-3}, respectively, and integrating over the 140-ps gate time of the x-ray imaging system, one finds $L_D \cong 175$ μm. Since the longitudinal IB absorption length is typically greater than 175 μm, heat diffusion is not expected to play a dominant role in determining the length of the x-ray emitting region.

In contrast, the nominal width of the focal spot is only 140 μm, that is, smaller than the characteristic thermal diffusion length. Therefore, some contribution from heat diffusion can be expected in this case. It should be noted, however, that the value of the nominal intensity of the interaction beam represents only an average value calculated assuming that the beam energy is uniformly distributed in the 140-μm focal spot during the 600-ps pulse duration.

The effect of the energy in the "wings" of the focal spot is therefore not accounted for in details by this simple description. However, we note that, as the laser pulse energy increases (decreases), the "effective" width of the focal spot that contributes to x-ray emission will consequently increase (decrease). Evidence of this effect is given by Fig. 9, which shows a sequence of time-resolved x-ray images of the laser–plasma interaction region obtained under conditions similar to those of Fig. 7, but at a lower interaction intensity of 3.5×10^{13} W/cm². The transverse size of the X-ray
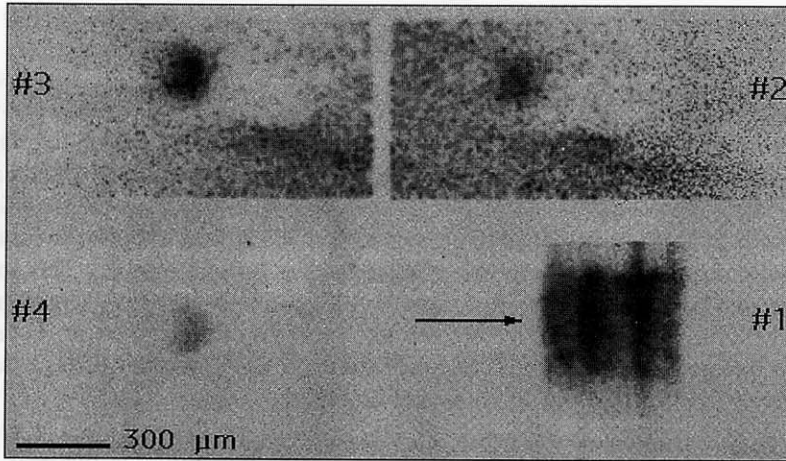
FIG. 9. Sequence of time resolved x-ray images of laser interaction with a preformed plasma produced under conditions analogous to those of Fig. 7, but at a lower interaction beam intensity 3.5 × 10¹³ W/cm². The arrow shows schematically the interaction beam configuration. The framing time was 120 ps, while the first interframe, that is the peak-to-peak delay between gate #1 and gate #2, was 2.2 ns, as shown in Fig. 6. The second and third interframes were zero and 100 ps, respectively.

region as shown in frame #3 is now approximately 150 μm compared to the 200 μm of frame #3 in Fig. 7.

The dependence of the width of the x-ray emitting region upon the laser intensity has been investigated in more detail and the result of this study is summarised in Fig. 10 that shows the width of the interaction region as measured from time-resolved x-
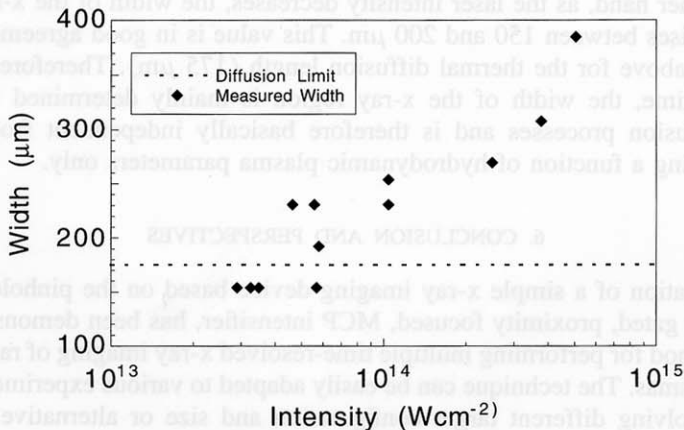

FIG. 10. Width of the x-ray emitting region as a function of the nominal intensity of the interaction beam focused on an Al plasma. The plasma heating intensity was approximately ≈4 × 10¹³ W/cm² on each side of the target. The horizontal dashed line indicates the limit set by the thermal diffusion length (175 μm) calculated under our experimental conditions.

ray images as a function of the interaction intensity in a range from 10^{13} to $\approx 10^{15}$ W/cm^2 obtained with the same 140-μm FWHM focal spot.

The first important feature of this graph is that, as the intensity increases, the transverse size also increases. This is consistent with the assumption made above that, in the high intensity limit, the width of the x-ray region can be mainly explained in terms of the contribution of the wings in the intensity distribution of the focal spot. Contribution to the spreading of the x-ray region may arise also from thermal diffusion processes. In fact, the energy of the interaction beam will heat the plasma locally and such heating will be increasingly important at higher laser intensities. This localised heating would give rise to enhanced thermal diffusion and the effect would increase with laser intensity. However, we believe that such an effect can be neglected with respect to the spreading due to the wings of the laser focal. In fact, if this effect was quantitatively important in our conditions, it should play a role in time-resolved images of Figures 7–9. Frames #2, #3, and #4 of these images show the x-ray region at different times during the interaction pulse, i.e., at the beginning, at the peak, and at the end of the pulse respectively, as described schematically in Fig. 6. The energy deposited in the plasma at each frame is increasingly higher, therefore a spreading driven by thermal diffusion should increase from a frame to the following. In contrast, no sizeable increase in the transverse spread of the x-ray region is measured when going from frame #2 to frame #4.

On the other hand, it is well known that, in the case of a steady state laser heating of underdense plasmas, the dependence of plasma temperature upon laser intensity is very weak, being described by a power law with exponent much smaller than one. Most of the energy absorbed by the plasma goes into kinetic energy, i.e., expansion and, in any case, the rate at which heat energy is diffused over the surrounding plasma is high enough to prevent large temperature increase of the irradiated plasma. In other words, the region of plasma irradiated by the interaction pulse effectively exhibits a relatively high heat capacity.

On the other hand, as the laser intensity decreases, the width of the x-ray emitting region stabilises between 150 and 200 μm. This value is in good agreement with the value given above for the thermal diffusion length (175 μm). Therefore, in the low intensity regime, the width of the x-ray region is mainly determined by classical thermal diffusion processes and is therefore basically independent from the laser intensity, being a function of hydrodynamic plasma parameters only.

6. CONCLUSION AND PERSPECTIVES

A combination of a simple x-ray imaging device based on the pinhole technique, coupled to a gated, proximity focused, MCP intensifier, has been demonstrated to be an ideal method for performing multiple time-resolved x-ray imaging of rapidly evolving laser plasmas. The technique can be easily adapted to various experimental configurations involving different target configuration and size or alternative laser beam setup, by simply changing the x-ray filter and by arranging the geometry of the primary imaging device (the pinhole array) in order to fit the required spectral properties of the image, as well as its resolution and magnification. In addition, the timing of each frame can easily be varied by simply adjusting the length of the cables that deliver

the high voltage pulses to each sensitive area of the detection unit. On the other hand, the number of the frames that can be obtained can also be varied by rearranging the design of the detection unit.

The experimental results presented here with a preliminary analysis and discussion, show how time-resolved x-ray imaging can provide valuable information of the physics of laser plasmas, which can be directly compared with the results of simple analytical models or with the predictions of numerical simulations. Fundamental aspects of the physics of laser–plasma interactions relevant to ICF studies including absorption processes and electron heat transport mechanisms can be investigated. In fact, the absorption length inferred from the x-ray images presented in this work was found to be in good agreement with the classical theory of linear collisional absorption. Furthermore, the thermal diffusion length estimated from the data was found to be consistent with the description provided by the classical thermal transport theory.

REFERENCES

1. T. Afshar-rad, L. A. Gizzi, M. Desselberger, F. Khattak, and O. Willi, *Phys. Rev. Lett.* **68,** 942 (1992).

2. K. S. Budil, T. S. Perry, P. M. Bell, J. D. Hares, P. L. Miller, T. A. Peyser, R. Wallace, H. Louis, and D. E. Smith, *Rev. Sci. Instrum.* **67,** 485 (1996).

3. L. Wiza, *Nucl. Instrum. Methods* **162,** 587 (1979).

4. O. Willi, *in* "Laser–Plasma Interactions 4, Proceedings of the 35th Scottish Universities' Summer School in Physics" (M. B. Hooper, Ed.), 1988.

5. J. D. Kilkenny, *Laser Part. Beams* **9,** 49 (1991).

6. D. K. Bradley, P. M. Bell, O. L. Landen, J. D. Kilkenny, and J. Oertel, *Rev. Sci. Instrum.* **66,** 716 (1995).

7. Kentech Instruments Ltd., Hall Farm Workshops, Didcot, UK.

8. R. W. Lee, L. Whitten, R. E. Stout II, *J. Quant. Spectr. Radiat. Trans.* **32,** 91 (1984).

9. L. A. Gizzi, Ph.D., thesis, Imperial College of Science, Technology and Medicine, 1994.

10. L. A. Gizzi, D. Giulietti, A. Giulietti, T. Afshar-rad, V. Biancalana, P. Chessa, C. Danson, E. Schifano, S. M. Viana, and O. Willi, *Phys. Rev. E* **49,** 5628 (1994).

11. L. Spitzer Jr., and R. Harm, *Phys. Rev.* **89,** 977 (1953).